N/S co-doped interconnected porous carbon nanosheets as high-performance supercapacitor electrode materials

WEI Yu-chen, ZHOU Jian, YANG Lei, GU Jing, CHEN Zhi-peng, HE Xiao-jun*

(*School of Chemistry and Chemical Engineering*, *Anhui Key Laboratory of Coal Clean Conversion and High Valued Utilization*, *Key Lab of Metallurgical Emission Reduction and Resources Recycling*, *Ministry of Education*, *Anhui University of Technology*, *Maanshan* 243002, *China*)

Abstract: The synthesis of porous carbon nanosheets without acid treatment for high-performance supercapacitors (SCs) is difficult. We report the construction of N/S co-doped porous carbon nanosheets (NS-PCNs) from coal tar pitch (CTP), using $Na_2S_2O_3·5H_2O$ as the sulfur source and K_2CO_3 as an activator, under flowing ammonia at high temperature. NS-IPCN$_{800}$ prepared at 800 °C is composed of two-dimensional (2D) nanosheets with abundant pores and an interconnected 3D carbon skeleton. The abundant microspores increase the number of active sites for electrolyte ion adsorption and small mesopores act as channels for fast ion transmission. The 3D carbon skeleton provides paths for electron conduction. Heteroatom doping provides an additional pseudocapacitance for the NS-IPCN electrodes. As a result the NS-IPCN$_{800}$ electrode has a high capacitance of 302 F g^{-1} at 0.05 A g^{-1} in a 6 mol L^{-1} of KOH electrolyte, and has a high energy density of 9.71 Wh kg^{-1} at a power density of 25.98 W kg^{-1}. It also has excellent cycling stability with a capacitance retention of over 94.2% after 10 000 charge-discharge cycles. This work suggests an environmentally friendly way to produce NS-IPCNs from CTP for use as high-performance SC electrode materials.

Key words: Coal tar pitch; N/S co-doped interconnected porous carbon nanosheets; Hierarchical pores; Supercapacitor

1 Introduction

Energy crisis and environmental pollution prompt the exploitation and utilization of clean energy sources such as solar energy and wind energy. However, these energy sources are unstable due to geographical and weather effects. Thus, it is urgent to develop efficient and green energy[1–4]. As clean energy storage devices, supercapacitors (SCs) have been widely concerned due to their rapid charge and discharge capability, long lifespan and high-power density[5–7]. However, the performance of SCs is mainly affected by electrode materials. The traditional electrode materials of SCs include porous carbons, metal oxides and organic conductive polymers[8]. Among them, porous carbons have drawn much attention because of their abundant resources and low cost[9–12]. Heteroatom doping is an effective method to increase capacitance of carbon materials by improving surface wettability and providing additional pseudocapacitance[13–16]. For example, N/S co-doped carbon material presented a specific capacitance of 169 F g^{-1} (10 A g^{-1}) [17]. Frustratingly, the preparation processes of porous carbons usually require acid or alkali for post-treatment, which inevitably increases environment pollution. In short, it is urgent to develop a no pickling method for synthesizing of carbon materials for high-performance SCs.

Coal tar pitch (CTP) is a by-product in the process of coal chemical industry. CTP can be used as precursors of porous carbon materials because of its cheapness and abundance[7]. In addition, CTP contains rich polycycle aromatic hydrocarbons, which are easy to be converted into graphene films at high temperatures[14]. Therefore, we report a no pickling method to synthesize N/S co-doped interconnected porous carbon nanosheets (NS-IPCNs) from CTP by using $Na_2S_2O_3·5H_2O$ as template and ammonia as dopant coupled with *in-situ* K_2CO_3 activation. The as-obtained NS-IPCN has three-dimensional (3D) structure composed of two-dimensional (2D) flakes with abundanthierarchical pores. Moreover, the N and S elements in IPCN provide additional pseudocapacitance[17]. As a result, NS-IPCN$_{800}$ electrode presents ex-

Received date: 2021-10-06; **Revised date:** 2021-12-09

Corresponding author: HE Xiao-jun, Professor. E-mail: xjhe@ahut.ed u.cn

Author introduction: WEI Yu-chen, Ph.D candidate. E-mail: wycglut@foxmail.com

Supplementary data associated with this article can be found in the online version.

cellent electrochemical performance due to its ultrathin sheet-like structure, reasonable pore size distribution and heteroatom doping. This study reports a no pickling method to construct NS-IPCNs from CTP for high-performance energy storage devices.

2 Experimental

2.1 Preparation of IPCNs

The CTP was reserved from Maanshan Iron & Steel Co. Ltd. Polytetrafluoroethylene (PTFE, purity, 50%) was purchased from DuPont Co. Ltd. of USA. Ammonia (purity, 99.99%) and Argon (purity, 99.99%) were purchased from Nanjing Specialty Gas Co. Ltd. of China. The purity of $Na_2S_2O_3·5H_2O$ and K_2CO_3 is 99.5% and 99%, respectively.

Firstly, 4 g of $Na_2S_2O_3·5H_2O$, 3 g of CTP and 12 g of K_2CO_3 were ground and mixed in the solid state. Secondly, the mixture was heated to 130 °C and kept for 30 min in flowing Ammonia (99.99%, 30 mL min^{-1}) and then heated to 800 °C for 60 min, followed by being cooled down to room temperature naturally at last. The obtained sample was washed several times with deionized water to ensure that the final filtrate was neutral, and dried at 110 °C for 24 h to obtain a product named as NS-$IPCN_{800,}$ where 800 represents final activation temperature. The samples synthesized at 750 and 850 °C were named as NS-$IPCN_{750}$ and NS-$IPCN_{850}$, respectively. Subsequently, the N-$IPCN_{800}$ was synthesized from 3 g of CTP and 12 g of K_2CO_3 in the absence of $Na_2S_2O_3·5H_2O$ at 800 °C. The S-$IPCN_{800}$ was prepared from 4 g of $Na_2S_2O_3·5H_2O$, 3 g of CTP and 12 g of K_2CO_3 in Argon atmosphere at 800 °C.

2.2 Characterization

The crystal powder of $Na_2S_2O_3·5H_2O$ was investigated by Thermogravimetric (TGA). The morphology of IPCNs was investigated by field emission scanning electron microcopy (FESEM, Nanosem430) and transmission electron microscopy (TEM, JEOL-2100). The pore structure parameters of IPCNs were obtained using N_2 adsorption/desorption at 77 K (Autosorb-IQ, Quantachrome, USA). The chemical bonding states of elements in IPCNs were analyzed by X-ray photo-electron spectroscopy (XPS, Thermo ESCALAB250, USA). The Raman spectra of IPCNs were recorded on Raman spectroscopy (JYLab-Ram HR800, excited by a 532 nm laser).

2.3 Electrochemical evaluation

The preparation process of the electrode is as below: (1) 90% IPCNs and 10% PTFE were mixed in deionized water; (2) the obtained mixture was dried into a paste substance; (3) the paste substance was rolled into thin carbon film and cut it into 6 mm of radius; (4) the carbon films were heated at 110 °C oven for 24 h under vacuum. The as-obtained carbon film was pressed onto foam nickel to fabricate electrode. The mass loading of active material for each electrode was about 2.0 mg cm^{-2}. Finally, the symmetrical button-type SCs were assembled with two similar electrodes separated by a polypropylene membrane in 6 mol L^{-1} of KOH electrolyte.

The cyclic voltammetry (CV) curves of SCs were obtained using an electrochemical workstation (CHI 760E, Shanghai Chenhua Instrument Co., Ltd.). The galvanostatic charge/discharge test (GCD) was investigated by SC test system on the Arbin Instruments (SCTS). The electrochemical impedance spectroscopy (EIS) was obtained on Power Transmission Impedance Analyzer (SI1260, Solartron Analytical, UK) with a frequency range of 10^{-3}–10^5 Hz. The specific capacitance (C_g, F g^{-1}) of the single IPCN electrode was calculated by the formula (1)[18].

$$C_g = 4I\Delta t/(m\Delta V) \quad (1)$$

Where I (A) represents the discharge current, Δt (s) is the discharge time, m (g) represents total mass of the active material in the two electrodes, ΔV (V) stands for the discharge voltage after IR drop.

The energy density (E, Wh kg^{-1}) and average power density (P, W kg^{-1}) of SCs were calculated according to equations (2) and (3)[19].

$$E = C_g V^2/28.8 \quad (2)$$

$$P = E/\Delta t_d \quad (3)$$

Where V (V) is the discharge voltage after IR drop and Δt_d (h) is the discharge time.

3 Results and discussion

Fig. 1 shows the direct fabrication of NS-IPCNs from CTP and the mechanism involved in the process. CTP, K_2CO_3 and $Na_2S_2O_3·5H_2O$ were ground and mixed homogeneously at first. The weight loss of $Na_2S_2O_3·5H_2O$ template was occurred at 20 to 140 °C due to the loss of crystalline water (Fig. S1(a), Supplementary Materials). In the subsequent heating step, CTP was liquefied at 150 °C, and then the small aromatic molecules in CTP were decomposed and reorganized to form an interconnected spherical film on the surface of the $Na_2S_2O_3$ template and K_2CO_3. Subsequently, $Na_2S_2O_3$ was decomposed to produce Na_2SO_4 and sodium polysulfide at 300 °C[20]. In addition, Na_2SO_4 and K_2CO_3 were involved the following chemical reactions with carbon in Eqs. (4-6)[21]. Simultaneously, the N and S elements in the raw materials were incorporated into carbon skeleton. The spherical film was broken to form an interconnected 3D sheet-like structure composed of ultrathin 2D nanosheets with rich hierarchical pores as the further increase of temperature. Finally, NS-IPCN was obtained after washing with deionized water.

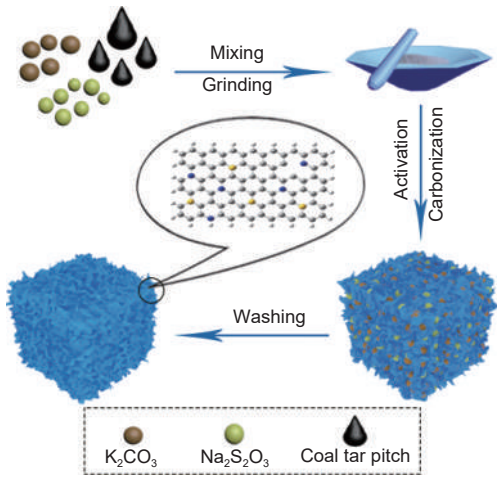

Fig. 1　Schematic diagram for the preparation of sheet-like NS-IPCNs from CTP.

$$Na_2SO_4 + 2C \rightarrow Na_2S + 2CO_2 \quad (4)$$

$$Na_2SO_4 + 4C \rightarrow Na_2S + 4CO \quad (5)$$

$$K_2CO_3 + 2C \rightarrow 2K + 3CO \quad (6)$$

The FESEM images of IPCNs in Fig. 2 (a-e) demonstrate the interconnected 3D structure. It is noted from Fig. 2b that NS-IPCN$_{800}$ with 3D interconnected structure was composed of ultrathin 2D carbon nanosheets with abundant hierarchical pores. The 3D interconnected structure not only improves the stability of carbon skeleton but also provides the highways for electrons transmission. More importantly, the pores on the flakes are expected to provide channels for electrolyte ion [22]. As shown in the TEM images (Fig. 2(d-e)), the thickness of NS-IPCN$_{800}$ carbon nanosheet is approximately 5 nm, which is thinner than that of NS-IPCN$_{750}$ and NS-IPCN$_{850}$. Short mesopores are easily formed in the thin nanosheets and are anticipated to shorten the transport distance of ion. Therefore, NS-IPCN$_{800}$ is one of the candidate electrode materials of SCs.

The N_2 adsorption/desorption isotherms of IPCNs in Fig. 3a are typical IV type with strong N_2 adsorption at the low relative pressure (p/p_0 < 0.01) and

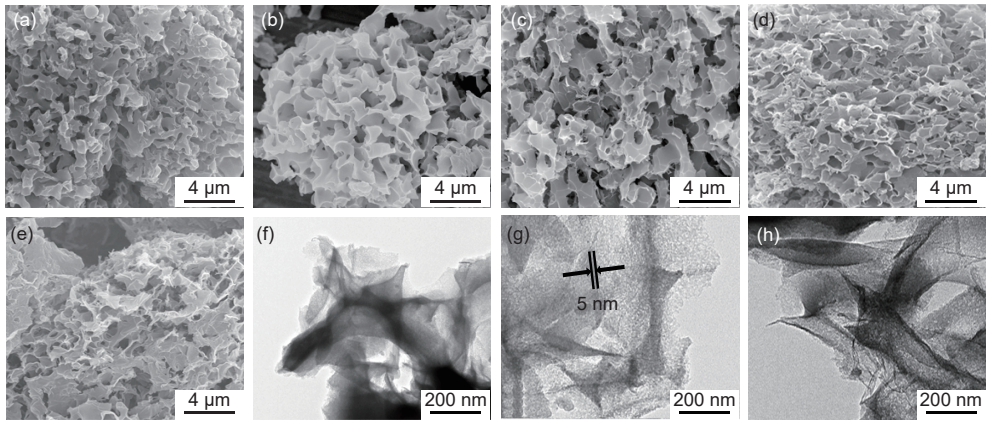

Fig. 2　FESEM images of (a) NS-IPCN$_{750}$, (b) NS-IPCN$_{800}$, (c) NS-IPCN$_{850}$, (d) N-IPCN$_{800}$ and (e) S-IPCN$_{800}$. TEM images of (f) NS-IPCN$_{750}$, (g) NS-IPCN$_{800}$ and (h) NS-IPCN$_{850}$.

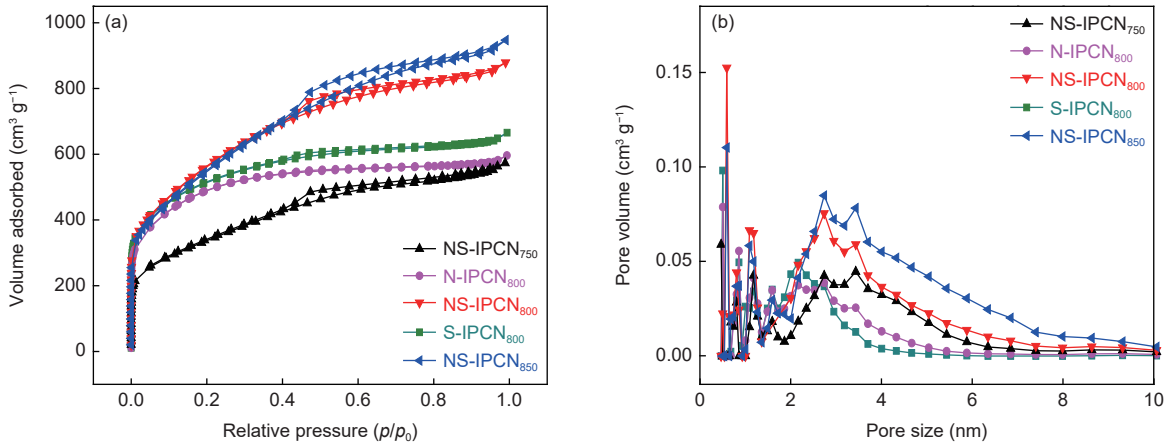

Fig. 3 (a) Nitrogen adsorption/desorption isotherms of IPCNs, (b) Micropores and part mesopores size distribution curves of IPCNs.

obvious hysteresis loops at $0.4 < p/p_0 < 0.95$, indicating the presence of abundant micropores and few mesopores in IPCNs. The micropores offer rich active sites for electrolyte ion adsorption, while mesopores are served as channels for ion transportation[22,23]. Fig. 3b and Fig. S1(b) show the detailed pore size distribution of IPCNs. The micropores of IPCNs center are at 0.6-1.2 nm, whereas the mesopores of IPCNs are mainly center at 2-5 nm. As the activation temperature enhances from 750 to 850 °C, the S_{BET} of IPCNs increases from 1 019 to 2 000 $m^2\ g^{-1}$ and then decreases to 1 977 $m^2\ g^{-1}$. The D_{ap} of IPCNs increases from 2.52 to 2.84 nm (Table 1). Additionally, the V_t of NS-IPCNs increases from 0.85 to 1.45 $cm^3\ g^{-1}$. These results indicate that the etching effect of K_2CO_3 on carbon skeleton increases with the increase of temperature, causing the micropores to collapse into mesopores.

Table 1 Pore structure parameters of IPCNs.

Samples	D_{ap} (nm)	S_{BET} ($m^2\ g^{-1}$)	V_t ($cm^3\ g^{-1}$)	V_{mic} ($cm^3\ g^{-1}$)
$NS\text{-}IPCN_{750}$	2.52	1019	0.85	0.38
$NS\text{-}IPCN_{800}$	2.63	2000	1.31	0.60
$NS\text{-}IPCN_{850}$	2.84	1977	1.45	0.45
$N\text{-}IPCN_{800}$	2.21	1622	0.88	0.21
$S\text{-}IPCN_{800}$	2.35	1682	0.98	0.28

D_{ap}: average pore diameter; S_{BET}: Brunauer–Emmett–Teller (BET) surface area; V_t: total pore volume; V_{mic}: micropores volume.

Fig. 4a presents the Raman spectra of IPCNs, showing the typical *D*-band at 1 340 cm^{-1} and *G*-band at 1 590 cm^{-1}. The *D* peak is related to the defects and disorder structure of the samples, while the *G* peak is assigned to the well-ordered graphitic structure[24]. The peak intensity ratios of I_D/I_G are 1.01 for $NS\text{-}IPCN_{750}$, 0.99 for $NS\text{-}IPCN_{800}$ and 0.94 for $NS\text{-}IPCN_{850}$, which are lower than that of graphene oxide of 1.02 [7], indicating that NS-IPCNs possess high degree of graphitization and therefore good conductivity.

The survey XPS spectra (Fig. 4b) of NS-IPCNs

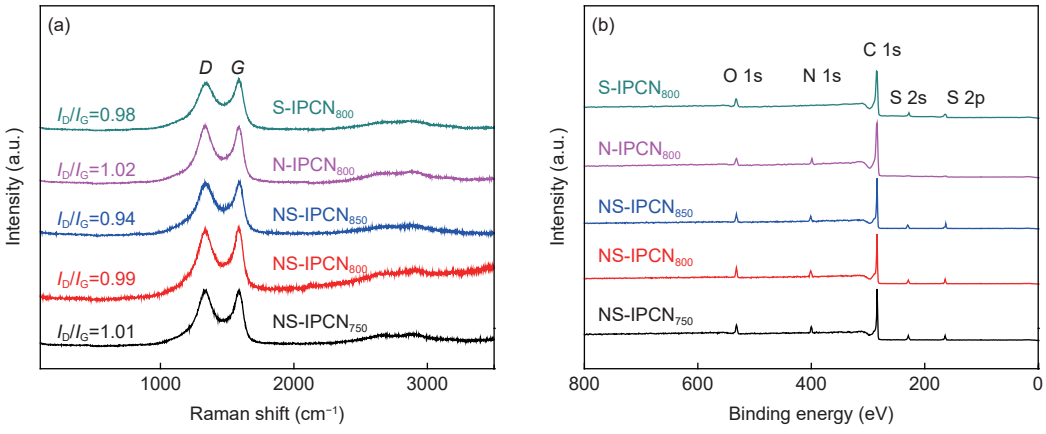

Fig. 4 (a) Raman spectra of IPCNs, (b) Full XPS spectra of IPCNs.

present two strong peaks at C 1s (285.1 eV), O 1s (532.5 eV) and three weak peaks at S 2s (228.4 eV), S 2p (164.3 eV) and N 1s (400 eV), showing that NS-IPCNs possess C, N, O and S elements. The O 1s spectra (Fig. S2) of IPNCs are deconvoluted into C=O (531.2 eV), C−O (532.6 eV) and −OH (536.1 eV) of oxygen-containing functional groups (Table 2). Oxygen-containing functional groups can improve the wettability of electrodes and reduce the diffusion resistance of electrolytes [15]. N 1s and S 2p spectra of IPCNs are exhibited in Fig. S3 and S4. The N 1s spectra of IPCNs can be fitted into four peaks (Table S1), including pyridinic nitrogen (N−6, 398.2 eV), pyrrolic-nitrogen (N−5, 399.99 eV), quaternary nitrogen (N−Q, 401.7 eV) and nitrogen oxide (NO_x, 403.5 eV). Among them, N−6 and N−5 can provide additional pseudocapacitance *via* the redox reaction on the surface of materials[25]. Moreover, N−5 and N −6 have favorable electron-donating properties, enhancing the charge transfer capability and the activities of NS-IPCNs[26,27]. In addition, N−Q and NO_x provide extra electrons for IPCNs, which can reduce the electron transfer barrier and improve the conductivity[28,29]. The S 2p spectra of IPCNs are resolved into three peaks, corresponding to SO_x (168.5 eV), S $2p_{1/2}$ (165.0 eV) and S $2p_{3/2}$ (163.5 eV) (Fig. S4 and Table S1). The introduced S elements are expected to increase structural defects of carbon skeleton and enhance the polarizability of atoms, further improving electrochemical activity[30].

Fig. 5a shows the CV curves of IPCNs at 10 mV s^{-1} in 6 mol L^{-1} of KOH electrolyte. The CV curves of all electrodes are quasi-rectangular shape without obvious redox peaks, indicating that IPCN electrodes have ideal electric double-layer capacitance (EDLC) behavior[13,31]. Fig. 5b and Fig. S5(a–d) present the CV curves of IPCN electrode at different scan rates. The curves exhibit approximately rectangular at a low scan rate. Moreover, the CV curve of NS-$IPCN_{800}$ still retains quasi-rectangular shape at 500 mV s^{-1}, proving the excellent rate performance of NS-$IPCN_{800}$ electrode. These results also indicate that the micropores in carbon material play a buffering role in ion migration by providing active sites for electrolyte adsorption and desorption[32,33].

The GCD curves of IPCN electrodes (Fig. 6a) present isosceles triangle, indicating the ideal EDLC behavior[19]. Obviously, the GCD time of NS-$IPCN_{800}$

Table 2　Contents of C, O, N and S elements in IPCNs.

Samples	C 1s (%)	O 1s (%)	N 1s (%)	S 2p (%)	O 1s		
					C=O (%)	C−O (%)	−OH (%)
NS-$IPCN_{750}$	89.63	7.53	1.99	0.84	4.44	3.08	0.01
NS-$IPCN_{800}$	93.95	4.63	0.99	0.43	2.41	2.21	0.01
NS-$IPCN_{850}$	94.92	3.88	0.87	0.33	2.01	1.86	0.01
N-$IPCN_{800}$	91.71	4.88	3.41	-	2.51	2.36	0.01
S-$IPCN_{800}$	90.64	6.45	-	3.04	3.43	3.01	0.01

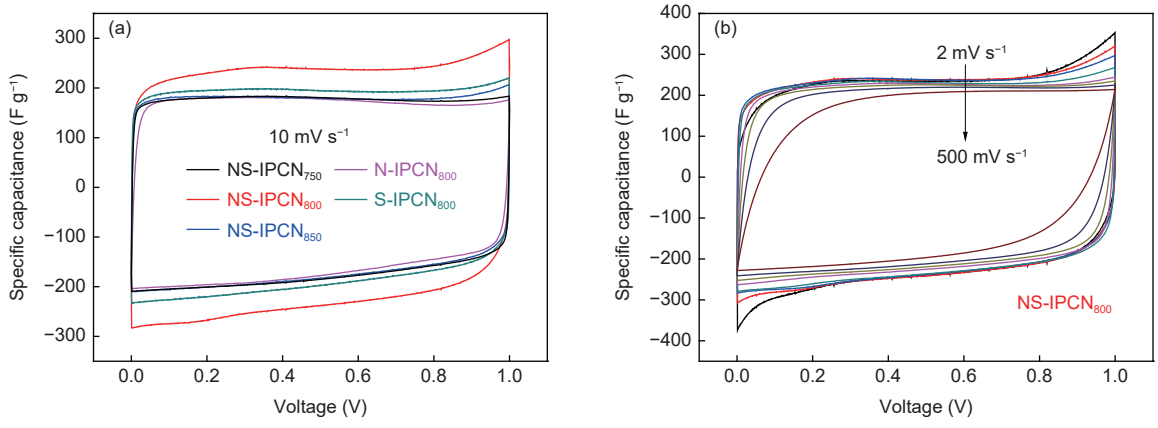

Fig. 5　(a) CV curves of IPCN electrodes at scan rate of 10 mV s^{-1} and (b) NS-$IPCN_{800}$ electrode at scan rates of 2-500 mV s^{-1}.

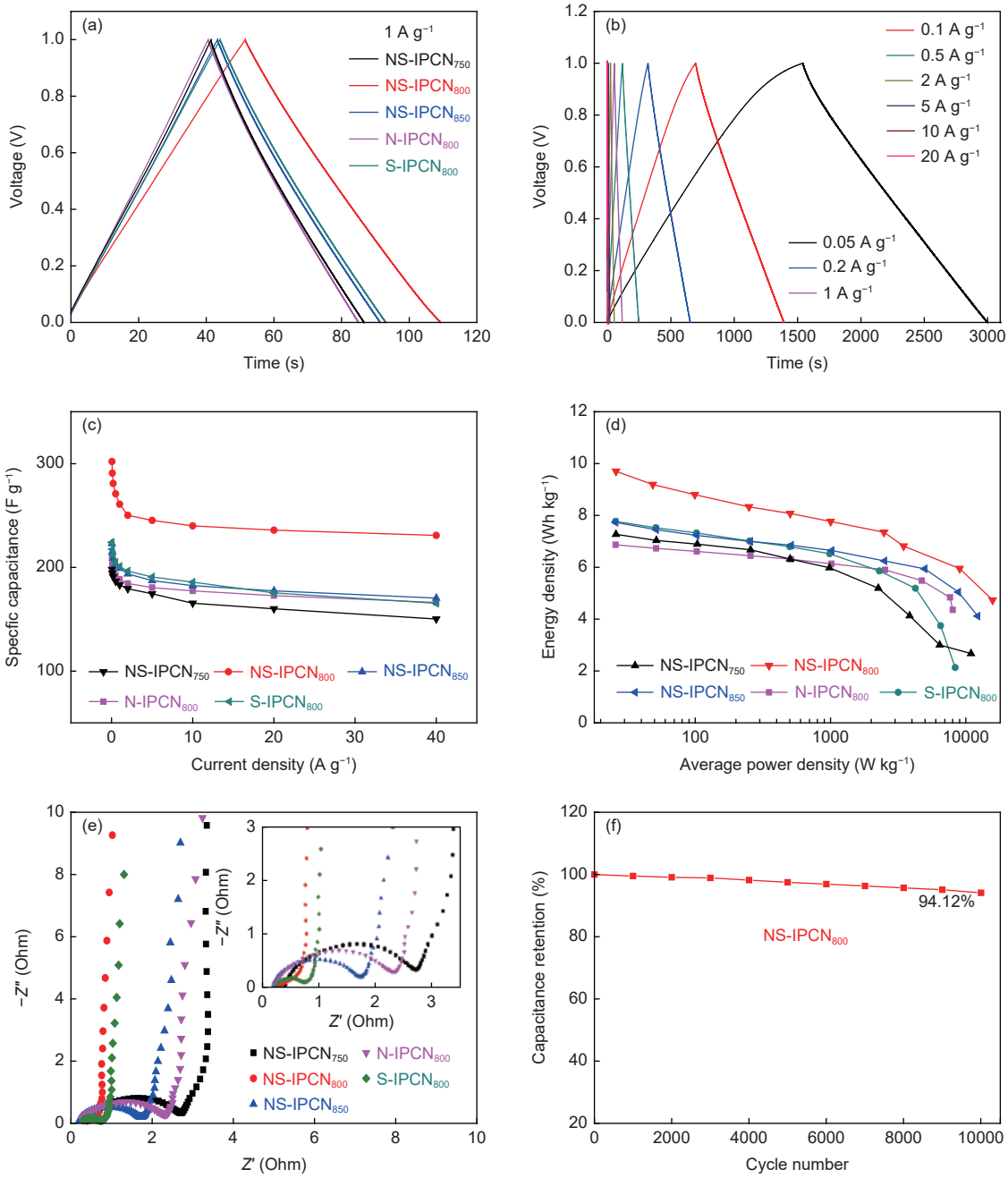

Fig. 6 (a) GCD curves of IPCN electrodes at 1 A g^{-1} in 6 mol L^{-1} of KOH electrolyte, (b) GCD curves of NS-$IPCN_{800}$ electrode at different current densities in 6 mol L^{-1} of KOH electrolyte, (c) Specific capacitance of IPCN capacitors at different current densities, (d) Ragone plots of IPCN capacitors, (e) Nyquist plots of IPCN capacitors, and (f) Cycle stability of NS-$IPCN_{800}$ capacitor measured at 5 A g^{-1}.

electrode is the longest, suggesting the highest specific capacitance. Fig. 6b shows the GCD curves of NS-$IPCN_{800}$ electrode. Fig. 6c demonstrates the specific capacitance curves of IPCN electrodes at various current density. The specific capacitance of NS-$IPCN_{800}$ electrode is 302 F g^{-1} at 0.05 A g^{-1}, which is higher than that of NS-$IPCN_{750}$ of 198 F g^{-1}, NS-$IPCN_{850}$ of 223 F g^{-1}, N-$IPCN_{800}$ of 210 F g^{-1} and S-$IPCN_{800}$ of 224 F g^{-1}. Similarly, the specific capacitance of NS-$IPCN_{800}$ electrode of 231 F g^{-1} is also higher than that of NS-$IPCN_{750}$ of 150 F g^{-1}, NS-$IPCN_{850}$ of 170 F g^{-1}, N-$IPCN_{800}$ of 166 F g^{-1} and S-$IPCN_{800}$ of 165 F g^{-1} at 40 A g^{-1}. The capacitance retention of NS-$IPCN_{800}$ capacitor reaches 76.5% with the increase of current density from 0.05 to 40 A g^{-1}. The specific capacitance of NS-$IPCN_{800}$ is higher than that of other electrodes reported in the literature (Table 3)[34–42].

Energy density is an important indicator of SCs[43].

Table 3　Comparison of the specific capacitance of NS-IPCN$_{800}$ electrode.

Sample	Electrolyte (mol L^{-1})	Current density (A g^{-1})	C_g (F g^{-1})	Energy density (Wh kg^{-1})	Ref.
PB/rGO	1.0 Na_2SO_4	0.3	286	45.4	[34]
GGI	6.0 KOH	0.5	301	9.1	[35]
Carbon nanobowls	6.0 KOH	0.1	279	9.6	[36]
ACS	6.0 KOH	1.0	208	9.2	[37]
HPCNT	6.0 KOH	0.1	286	8.45	[38]
SNPCNs	6.0 KOH	0.5	286	5.9	[39]
RGO	1.0 Na_2SO_4	0.5	147.5	3.3	[40]
HGNs	6.0 KOH	1.0	295	9.4	[41]
NPS-HCS	6.0 KOH	0.5	274	8.4	[42]
NS-IPCN$_{800}$	6.0 KOH	0.05	302	9.71	This work

Fig. 6d reflects the energy density of IPCN capacitors at different power densities. The energy density of NS-IPCN$_{800}$ capacitor of 9.71 Wh kg^{-1} at a power density of 25.98 W kg^{-1} is significantly higher than that of NS-IPCN$_{750}$ (7.27 Wh kg^{-1}) and NS-IPCN$_{850}$ (7.73 Wh kg^{-1}). The ideal Nyquist diagram is a straight line perpendicular to the Z' axis[44,45]. In the low-frequency region, the Nyquist diagram of IPCN capacitor is almost perpendicular to the Z' axis, indicating the ideal EDLC characteristics. The x-intercept of the Z' axis corresponds to the intrinsic ohmic resistance (R_s) of IPCN capacitors, while the diameter of semicircle represents the charge transfer resistance (R_{ct})[46]. The R_s and R_{ct} of NS-IPCN$_{800}$ capacitor of 0.19 and 0.42 Ω are the smallest among the five IPCN capacitors (Fig. 6e), demonstrating that NS-IPCN$_{800}$ electrode possesses better electronic conductivity and lower resistance. Cycle stability is another important indicator for the practical application of SCs. Fig. 6f shows that the capacitance retention of NS-IPCN$_{800}$ capacitor maintains 94.12% at 5 A g^{-1} after 10 000 cycles. The excellent cycle stability confirms that NS-IPCN$_{800}$ is very suitable as electrode material for long-lifespans SCs.

4　Conclusion

In summary, N/S co-doped IPCNs are prepared from CTP with $Na_2S_2O_3 \cdot 5H_2O$ as template and ammonia as dopant coupled with *in-situ* K_2CO_3 activation. The as-prepared NS-IPCN$_{800}$ features interconnected 3D structure is composed of 2D ultrathin nanosheets with rich hierarchical pores. In addition, NS-IPCN$_{800}$ possesses a high degree of graphitization and a good conductivity. Besides, the moderate heteroatom doping provides additional pseudocapacitance for NS-IPCN$_{800}$ electrodes. Benefitting from these merits, NS-IPCN$_{800}$ electrode exhibits excellent electrochemical performance such as high specific capacitance of 302 F g^{-1} at 0.05 A g^{-1} and excellent rate performance of 230 F g^{-1} at 40 A g^{-1}. Additionally, NS-IPCN$_{800}$ capacitor presents high cycle stability with only 5.88% decay after 10 000 cycles at 5 A g^{-1}. This work provides a simple method without pickling to construct high-performance electrode materials from CTP for energy storage devices, realizing the high added utilization of chemical by-products.

Acknowledgement

The authors acknowledge the financial support from the National Natural Science Foundation of China (52072002, 51872005, U1710116 and U1508201) and the WanJiang Scholar Program.

References

[1] Deng W W, Qian J F, Cao Y L, et al. Graphene-wrapped $Na_2C_{12}H_6O_4$ nanoflowers as high-performance anodes for sodium-ion batteries[J]. Small, 2016, 12: 583-587.

[2] Kajiyama S, Szabova L, Sodeyama K, et al. Sodium-ion intercalation mechanism in MXene nanosheets[J]. ACS Nano, 2016, 10: 3334-3341.

[3] Qiu X, Wang N, Wang Z, et al. Towards high-performance zinc-based hybrid supercapacitors via macropores-based charge storage in organic electrolytes[J]. Angewandte Chemie International Edition, 2021, 60: 9610-9617.

[4] Feng J Z, Wang Y, Xu Y T, et al. Construction of supercapacitor-based ionic diodes with adjustable bias directions by using poly (ionic liquid) electrolytes[J]. Advanced Materials, 2021, 24:

2100887.

[5] Jayaramulu K, Dubal D P, Nagar B, et al. Ultrathin hierarchical porous carbon nanosheets for high-performance supercapacitors and redox electrolyte energy storage[J]. Advanced Materials, 2018, 30: 1705789.

[6] Lee J H, Chae J S, Jeong J H, et al. An ionic liquid incorporated in a quasi-solid-state electrolyte for high-temperature supercapacitor applications[J]. Chemical Communications, 2019, 55: 15081-15084.

[7] He X J, Zhang H B, Zhang H, et al. Direct synthesis of 3D hollow porous graphene balls from coal tar pitch for high performance supercapacitors[J]. Journal of Materials Chemistry A, 2014, 2: 19633-19640.

[8] Simon P, Gogotsi Y, Dunn B. Where do batteries end and supercapacitors begin?[J]. Science, 2014, 343: 1210-1211.

[9] Rafieerad A, Amiri A, Sequiera L G, et al. Development of fluorine-free tantalum carbide MXene hybrid structure as a biocompatible material for supercapacitor electrodes[J]. Advanced Functional Materials, 2021, 31: 2100015.

[10] Liu Y C, Hung Y H, Sutarsis, et al. Effects of surface functional groups of coal-tar-pitch-derived nanoporous carbon anodes on microbial fuel cell performance[J]. Renewable Energy, 2021, 171: 87-94.

[11] Zang L M, Liu Q F, Qiu J H, et al. Design and fabrication of an all-solid-state polymer supercapacitor with highly mechanical flexibility based on polypyrrole hydrogel[J]. ACS Applied Materials Interfaces, 2017, 9: 33941-33947.

[12] Liang X, Nie K W, Ding X, et al. Highly compressible carbon sponge supercapacitor electrode with enhanced performance by growing nickel-cobalt sulfide nanosheets[J]. ACS Applied Materials Interfaces, 2018, 10: 10087-10095.

[13] Wei F, Zhang H F, He X J, et al. Synthesis of porous carbons from coal tar pitch for high-performance supercapacitors[J]. New Carbon Materials, 2019, 34: 132-139.

[14] He X J, Zhang N, Shao X L, et al. A layered-template-nanospace-confinement strategy for production of corrugated graphene nanosheets from petroleum pitch for supercapacitors[J]. Chemical Engineer Journal, 2016, 297: 121-127.

[15] Ma T, Liao L X, Zhang X, et al. Hierarchical pores from microscale to macroscale boost ultrahigh lithium intercalation pseudo-capacitance of biomass carbon[J]. Journal of Energy Storage, 2021, 33: 102068.

[16] Deshagani S, Maity D, Das A, et al. $NiMoO_4$@$NiMnCo_2O_4$ heterostructure: A poly (3, 4-propylenedioxythiophene) composite-based supercapacitor powers an electrochromic device[J]. ACS Applied Materials Interfaces, 2021, 13: 34518-34532.

[17] Sun L, Zhou H, Li L, et al. Double soft-template synthesis of nitrogen/sulfur-codoped hierarchically porous carbon materials derived from protic ionic liquid for supercapacitor[J]. ACS Applied Materials Interfaces, 2017, 9: 26088-26095.

[18] Chen M H, Fan H, Zhang Y, et al. Coupling PEDOT on mesoporous vanadium nitride arrays for advanced flexible all-solid-state supercapacitors[J]. Small, 2020, 16: 2003434.

[19] Zhang P P, Wang M C, Liu Y N, et al. Dual-redox-sites enable two-dimensional conjugated metal-organic frameworks with large pseudocapacitance and wide potential window[J]. Journal of the American Chemical Society, 2021, 143: 10168-10176.

[20] Fu W W, Zou T, Liang X H, et al. Characterization and thermal performance of microencapsulated sodium thiosulfate pentahydrate as phase change material for thermal energy storage[J]. Solar Energy Materials Solar Cells, 2019, 193: 149-156.

[21] Pang J, Zhang W F, Zhang J L, et al. Facile and sustainable synthesis of sodium lignosulfonate derived hierarchical porous carbons for supercapacitors with high volumetric energy densities[J]. Green Chemistry, 2017, 19: 3916-3926.

[22] He T, Huang Z H, Yuan S, et al. Kinetically controlled reticular assembly of a chemically stable mesoporous Ni(II)-pyrazolate metal-organic framework[J]. Journal of the American Chemical Society, 2021, 142: 13491-13499.

[23] Sun H H, Liu H Y, Hou Z D, et al. Edge-terminated MoS_2 nanosheets with an expanded interlayer spacing on graphene to boost supercapacitive performance[J]. Chemical Engineering Journal, 2020, 387: 124204.

[24] Lv T, Liu M X, Zhu D Z, et al. Nanocarbon-based materials for flexible all-solid-state supercapacitors[J]. Advanced Materials, 2018, 30: 1705489.

[25] Zhao X, Wang S J, Wu Q. Nitrogen and phosphorus dual-doped hierarchical porous carbon with excellent supercapacitance performance[J]. Electrochimica Acta, 2017, 247: 1140-1146.

[26] Qi F L, Xia Z X, Wei W, et al. Nitrogen/sulfur co-doping assisted chemical activation for synthesis of hierarchical porous carbon as an efficient electrode material for supercapacitors[J]. Electrochimica Acta, 2017, 246: 59-67.

[27] Wan L, Wang J L, Xie L J, et al. Nitrogen-enriched hierarchically porous carbons prepared from polybenzoxazine for high-performance supercapacitors[J]. ACS Applied Materials Interfaces, 2014, 6: 15583-15596.

[28] Ran F T, Yang X B, Xu X Q, et al. Green activation of sustainable resources to synthesize nitrogen-doped oxygen-riched porous carbon nanosheets towards high-performance supercapacitor[J]. Chemical Engineering Journal, 2021, 412: 128673.

[29] Lo C T, Lin K W, Wang T P, et al. Differentiating between the effects of nitrogen plasma and hydrothermal treatment on electrospun carbon fibers used as supercapacitor electrodes[J]. Electrochimica Acta, 2021, 381: 138255.

[30] Yang P H, Mai W J. Flexible solid-state electrochemical supercapacitors[J]. Nano Energy, 2014, 8: 274-290.

[31] Xu K L, Liu J, Yan Z X, et al. Synthesis and use of hollow carbon spheres for electric double-layer capacitors[J]. New Carbon Materials, 2021, 36: 794-809.

[32] Benzigar R M, Talapaneni N S, Joseph S, et al. Recent advances in functionalized micro and mesoporous carbon materials: synthesis and applications[J]. Chemical Society Reviews, 2018, 47: 2680-2721.

[33] He X J, Xie X Y, Wang J X, et al. From fluorene molecules to

ultrathin carbon nanonets with an enhanced charge transfer capability for supercapacitors[J]. Nanoscale, 2019, 11: 6610-6619.

[34] Wang J G, Ren L B, Hou Z D, et al. Flexible reduced graphene oxide/prussian blue films for hybrid supercapacitors[J]. Chemical Engineering Journal, 2020, 397: 125521.

[35] Yan Y, Hao X F, Gao L G, et al. Highly accessible hierarchical porous carbon from a bi-functional ionic liquid bulky gel: High-performance electrochemical double layer capacitors[J]. Journal of Materials Chemistry A, 2019, 7: 25297.

[36] Wang J G, Liu H Z, Zhang X Y, et al. Elaborate construction of N/S-co-doped carbon nanobowls for ultrahigh-power supercapacitors[J]. Journal of Materials Chemistry A, 2018, 6: 17653.

[37] Zhang X, Wang Y Z, Yu X W, et al. High-performance discarded separator-based activated carbon for the application of supercapacitors[J]. Journal of Energy Storage, 2021, 44: 103378.

[38] Wang J G, Liu H Z, Zhang X Y, et al. Green synthesis of hierarchically porous carbon nanotubes as advanced materials for high-efficient energy storage[J]. Small, 2018, 4: 1703950.

[39] Chen C, Zhao M K, Cai Y Y, et al. Scalable synthesis of strutted nitrogen doped hierarchical porous carbon nanosheets for supercapacitors with both high gravimetric and volumetric performances[J]. Carbon, 2021, 179: 458-468.

[40] Oyedotun K O, Masikhwa T M, Lindberg S, et al. Comparison of ionic liquid electrolyte to aqueous electrolytes on carbon nanofibres supercapacitor electrode derived from oxygen-functionalized graphene[J]. Chemical Engineering Journal, 2019, 375: 121906.

[41] Wang J, Park T, Yi J W, et al. Scalable synthesis of holey graphite nanosheets for supercapacitors with high volumetric capacitance[J]. Nanoscale Horizons, 2019, 4: 526-530.

[42] Yan L J, Li D, Yan T T, et al. N, P, S-codoped hierarchically porous carbon spheres with well-balanced gravimetric/volumetric capacitance for supercapacitors[J]. ACS Sustainable Chemistry Engineering, 2018, 6: 5265-5272.

[43] Wei F, He X J, Ma L B, et al. 3D N, O-codoped egg-box-like carbons with tuned channels for high areal capacitance supercapacitors[J]. Nano-Micro Letters, 2020, 12: 82.

[44] Choi J, Nam D, Shin D, et al. Charge-transfer-modulated transparent supercapacitor using multidentate molecular linker and conductive transparent nanoparticle assembly[J]. ACS Nano, 2019, 13: 12719-12731.

[45] Cai D, Lu M J, Li L, et al. A highly conductive MOF of graphene analogue $Ni_3(HITP)_2$ as a sulfur host for high-performance lithium-sulfur batteries[J]. Small, 2019, 15: 1902605.

[46] Yang F, Zhang S K, Yang Y, et al. Heteroatoms doped carbons derived from crosslinked polyphosphazenes for supercapacitor electrodes[J]. Electrochimica Acta, 2019, 328: 135064.